PHOTONICS Research

Integrated topological photonic circuit for on-chip second-harmonic generation and frequency demultiplexing

Chunlin Ma, Junhao Yang, Chenyang Peng, Gang Li, Shaojie Xue, and Xinyuan Qi*

School of Physics, Northwest University, Xi'an 710127, China
**Corresponding author: qixycn@nwu.edu.cn*

Received 23 July 2025; revised 30 September 2025; accepted 30 October 2025; posted 11 November 2025 (Doc. ID 573858); published 30 January 2026

We propose a monolithic topological photonic circuit that integrates second-harmonic generation (SHG) and wavelength demultiplexing in a single platform. Leveraging the finite element method (FEM) for electromagnetic simulations, a sandwich waveguide heterostructure with air-gap-tuned edge states simultaneously generates SHG at 280.6 THz and routes fundamental (FW) and second-harmonic waves (SHW) through topologically distinct paths: FW propagates via a nontrivial edge state (near-zero backscattering), while SHW transmits through a trivial boundary mode (optimized dispersion). Simulated results demonstrate greater than 99.88% separation efficiency —matching the state-of-the-art in topological isolation systems. The dual-functionality design eliminates hybrid-component losses, yielding a normalized SHG efficiency of $\eta = 139.4\%\ \mathrm{W}^{-1}\ \mathrm{cm}^{-2}$. Field profiles confirm that the spatial isolation of FW/SHW outputs a minimum crosstalk suppression of −29.2 dB. This work establishes a scalable paradigm for topology-enabled nonlinear light management in quantum frequency conversion and photonic signal processing.

https://doi.org/10.1364/PRJ.573858

1. INTRODUCTION

The relentless pursuit of miniaturized photonic circuits for on-chip optical signal processing has spurred significant interest in nonlinear frequency conversion and wavelength-division multiplexing (WDM) technologies [1–3]. Second-harmonic generation (SHG), as a fundamental nonlinear process, enables critical applications in quantum light sources [4], ultrafast modulation [5], and frequency metrology [6]. However, conventional nonlinear photonic devices face persistent challenges in integrating SHG with efficient frequency sorting, primarily due to insertion losses at hybrid interfaces and sensitivity to fabrication disorders [7]. Topological photonics, with its hallmark defect-immune light transport, offers a promising platform to overcome these limitations [8–10].

Recent years have witnessed remarkable progress in topological photonic crystals (PhCs), where robust edge states protected by topological invariants enable backscattering-suppressed light propagation [11]. Pioneering works by Haldane and Raghu [12] established the theoretical foundation, followed by experimental realizations of diverse topological phases, including quantum Hall [13,14], valley Hall [15–17], and higher-order topological states [18,19]. Besides, studies in silicon topological photonics showcase robust devices like valley-locked heterostructure waveguides, power splitters, and ring resonators for on-chip filtering, offering defect immunity and high performance [20–22]. Furthermore, advancements include enhanced nonlinear harmonics in nanocavity chains and Fano resonances in 1D topological photonic crystals, enabling strong light–matter interactions [23,24]. These advances have naturally extended to nonlinear regimes: topological edge [25,26] and corner states [27–29] enhance SHG through strong field confinement and extended interaction lengths. For instance, Lan *et al.* demonstrated topology-protected nonlinear frequency conversion via one-way edge modes of topological PhCs by tailoring the geometry of the edge termination [25], and Guo *et al.* achieved enhanced conversion using topological corner resonators [29], while Hu *et al.* achieved SHG in a topological cavity by matching the phase distributions of the electric fields of the topological corner state and topological edge state [30]. Nevertheless, these systems lack integrated frequency demultiplexing—a crucial functionality for practical nonlinear light sources. Existing frequency dividers based on Mach–Zehnder interferometers [31–33] or Bragg gratings [34–36] exhibit high losses (>3 dB) and limited bandwidth, and they cannot be monolithically integrated with topological SHG elements due to mode mismatch and disorder sensitivity.

Here, we bridge this gap through a monolithic topological photonic circuit that integrates second-harmonic generation

Corrected 11 February 2026

and wavelength demultiplexing within a single heterostructure. Our design leverages complementary topological edge states—nontrivial for robust fundamental wave transport to Port 2 and trivial for second-harmonic routing to Port 3—enabling dual-boundary SHG enhancement via C_6-symmetry-broken waveguides. By incorporating air-gap dispersion engineering to spectrally align FW/SHW bands, we achieve greater than 99.88% separation efficiency with minimum crosstalk suppression of −29.2 dB. Simulations with FEM at 140.3/280.6 THz confirm $\eta = 139.4\%\ \mathrm{W}^{-1}\,\mathrm{cm}^{-2}$, demonstrating the first unified platform for topological nonlinear light management.

2. MODEL AND THEORY

Our two-dimensional (2D) complex hexagonal photonic crystal [Fig. 1(a)] consists of two types of distinct triangular dielectric cylinders in each unit cell, featuring concentric inner and outer triangular geometries with side lengths l and d, respectively [Fig. 1(c1) or 1(d1)]. The periodicity of the PhCs is $a = 775$ nm. The dielectric cylinders ($\varepsilon = 12$) exhibit second-order nonlinear susceptibility $\chi^{(2)} = 10^{-21}$ C/V^2, while air forms the background medium. The size asymmetry ($l \neq d$) breaks C_6 rotational symmetry while maintaining translational periodicity.

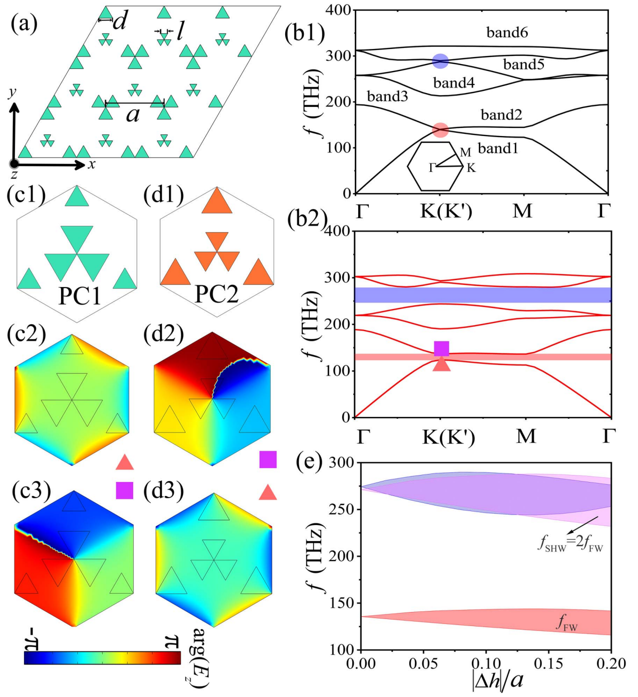

Fig. 1. Structures and transverse magnetic (TM) bands. (a) Complex hexagonal topological photonic crystal, with (c1), (d1) the inner triangular side length of l and the outer triangular side length of d. (b1) Band structure for $(d_0, l_0) = (0.22a, 0.22a)$. (b2) Band structure for $(d_1, l_1) = (0.2a, 0.27a)$ or $(d_2, l_2) = (0.27a, 0.2a)$. (c1), (d1) Unit cells of PC1 and PC2, respectively. (c2), (c3) Calculated phases in the band structure of the triangle and pentagram with (d_1, l_1). (d2), (d3) Calculated phases in the band structure of the triangle and pentagram with $(d_2, l_2) = (0.27a, 0.2a)$. (e) Calculated maps of the first and second bandgaps versus $|\Delta h|/a$ for the K point.

We investigated the TM photonic bands of our composite hexagonal crystal, observing a Dirac point between bands 1 and 2 at the K point in the symmetric case ($d_0 = l_0 = 0.22a$) [Fig. 1(b1)]. Introducing asymmetry ($l \neq d$) lifts this degeneracy: bandgaps between bands 1 and 2, bands 4 and 5 open, respectively, for both $l < d$ and $l > d$ configurations. For the case of $(d_1, l_1) = (0.2a, 0.27a) = (l_1, d_1)$, the band structure is shown in Fig. 1(b2), and the phase distributions of E_z at K are shown in Figs. 1(c2) and 1(c3). Compared with the results for the case of $(d_2, l_2) = (0.27a, 0.2a)$ [Figs. 1(d2) and 1(d3)], the vorticities are reversed [Figs. 1(c2) and 1(d3)]—indicating that the topologies are distinct. Further phase analysis of modes in bands 4 and 5 confirmed topological triviality (see Fig. 6 in Appendix A), while Berry phase calculations established nontrivial topology for bands 1 and 2, as detailed in Fig. 7 of Appendix A. Systematic $|\Delta h| = |d - l|$ tuning—with d incremented by $0.01a$ and l decremented by $0.01a$—reveals critical spectral overlap (>80%) between the two types of first bandgap frequency domain (purple) and second bandgap (blue) [Fig. 1(e)], showing the significant feasibility of efficient phase-matched SHG through simultaneous FW/SHW confinement.

Employing the distinct topologic phases of unit cells [Figs. 1(c1) and 1(d1)] and the bulk-edge correspondence, we constructed two types of supercells, PC1-PC2 and PC2-PC1, with their enlarged interface structures shown in Figs. 2(a) and 2(b), respectively. The calculated dispersion curves indicate that the PC1-PC2 supercell supports topological edge states in the first bandgap, while PC2-PC1 exhibits non-topological boundary states in the second bandgap [Figs. 2(b) and 2(e)]. The simulated transmission results show that frequencies satisfying $f_{\mathrm{SHW}} = 2f_{\mathrm{FW}}$ at $k_x a/\pi = -0.72$ [purple/green markers in Figs. 2(b) and 2(e)] exhibit strong localization at respective interfaces [Figs. 2(c) and 2(f)], which means a sandwich structure combined by these two supercells might construct a monolithic topological photonic chip for both the SHG and WDM. Note that the other two bandgap cases of the supercell are not applicable for the SHG as explained in detail in Fig. 8 of Appendix B.

3. SECOND-HARMONIC GENERATION AND SEPARATION

In the following, we constructed a sandwich-structure photonic circuit to simultaneously enable SHG and WDM. Initially, the side lengths of the inner and outer triangular geometries were chosen to be (d_2, l_3) for PC1 and $(d, l) = (l_3, d_2)$ for PC2. Although the simulated propagation dynamics reveal comparable SHG conversion efficiencies near the sources (around the position of $z = 0$), FW (around 135.63 THz) undergoes rapid attenuation and dissipation once it enters the PhCs, as FW lies precisely within the forbidden band (see Fig. 9, Appendix B).

To enable simultaneous SHG and co-propagation of FW/SHW in the sandwich waveguide, we optimized wavevector matching and lattice geometry to resolve the inherent trade-off between SHG efficiency (requiring spatial overlap [37]) and frequency separation. Our approach strategically balances topological and trivial boundary states across distinct spectral

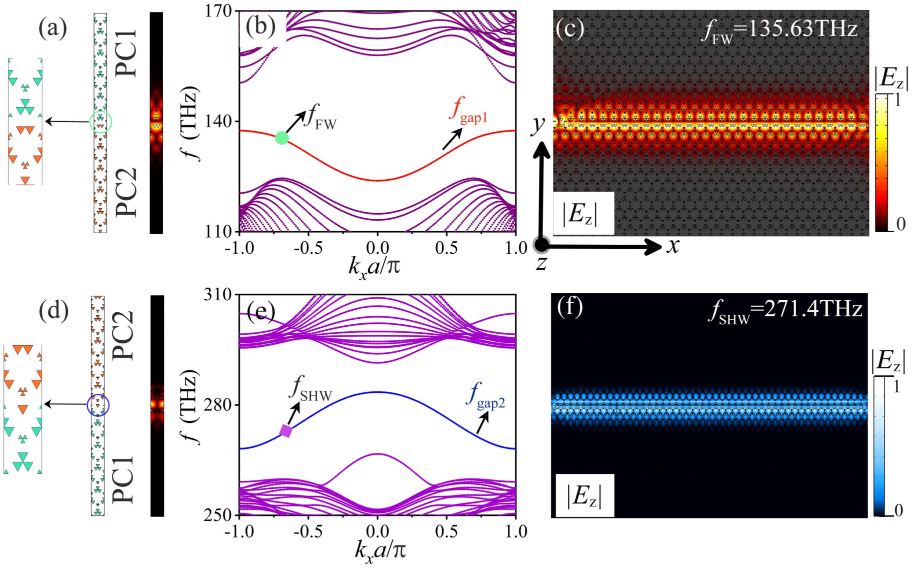

Fig. 2. Calculated dispersion curves and transmission when $(d_2, l_3) = (0.27a, 0.12a)$. (a), (d) Supercell and electric field. (b) The first band of (a). (c) The second dispersion of (d). (e), (f) Transmission in photonic crystal (a) and (d).

regions. The solution requires satisfying two conditions simultaneously. (1) The SHG phase matching condition is determined by the intersections of the topological edge state curves [red dotted curve, (PC1-PC2): $2f_{\mathrm{gap1}}$ or orange dotted curve, (PC2-PC1): $2f_{\mathrm{gap1}}$ in Fig. 3(a)] and the non-topological edge state curves [blue dotted curve, (PC2-PC1): f_{gap2} or green dotted curve, (PC1-PC2): f_{gap2} in Fig. 3(a), as indicated by the light blue hollow pentagon, red hollow hexagon, and blue triangle in Fig. 3(a). (2) The frequency separation is governed by the frequency difference between the maximum value of the topological states [orange dotted curve, (PC2-PC1): $2f_{\mathrm{gap1}}$ in Fig. 3(a)] and the minimum one of the non-topological states [green dotted curve, (PC1-PC2): f_{gap2} in Fig. 3(a)]. Therefore, the required frequencies must lie within the gray region between the minimum point ($k_xa = -\pi$) on the orange dotted curve and the maximum point ($k_xa = -\pi$) on the green dotted curve in Fig. 3(a). Optimal operation occurs where these two conditions overlap [the hollow pentagons in the shaded region, Fig. 3(a)].

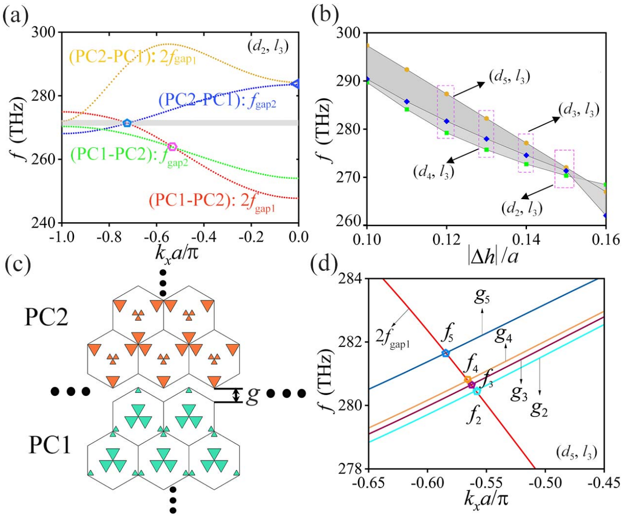

Fig. 3. Optimization of the geometric structure parameters required for the simultaneous achievement of phase matching and frequency separation. (a) Combined dispersion curves from Figs. 2(a) and 2(d). (b) Dispersion versus $\Delta h/a$ for $d_{2\text{–}5} = [0.27, 0.26, 0.25, 0.24]a$ and $l_3 = 0.12a$. Orange circles/green squares: values at $k_xa = -\pi$ in (a). Blue boxes: intersection points of blue/red dotted curves in (a). (c) Schematic of topological photonic crystal with air gap g. (d) FW/SHW dispersion for (d_5, l_3) with gap variations. Pentagrams $f_5 - f_2$: intersections at $g_5 = 0$ (red/blue), $g_4 = \sqrt{2}d_5/7$ (red/yellow), $g_3 = \sqrt{2}d_5/6$ (red/dark purple), $g_2 = \sqrt{2}d_5/5$ (red/light blue). Shaded regions in (a), (b) indicate operational domains for simultaneous FW/SHW generation and separation.

Through parameter tuning (l fixed at $l_3 = 0.12a$, d varied as $d_0 + 0.01a$), we mapped frequency versus $|\Delta h| = |d - l|$ [Fig. 3(b)]. The orange circles and green squares in Fig. 3(b) represent the frequencies at $k_xa = -\pi$ in Fig. 3(a). The blue boxes in Fig. 3(a) represent the intersection points for the SHG phase matching. Three candidate points (purple boxes) within the target region showed promising spectral alignment but exhibited suboptimal transmission (see Fig. 12, Appendix D), necessitating interface engineering. Although the geometric conditions of (d_5, l_3) allow for relatively favorable localized optical transmission and SHG efficiency, the structural design still remains to be further optimized.

To overcome the limitations identified in the initial sandwich structure, we introduced an air layer of width g at the PC2-PC1 interface as shown in Fig. 3(c). This air-gap engineering was implemented for structures with fixed parameters $l_3 = 0.12a$ and $d_5 = 0.24a$. Systematic tuning of g [Fig. 3(d)] demonstrated that increasing the air gap progressively red shifts the SHW frequencies ($f_5 \approx 281.65$ THz to $f_2 \approx 280.46$ THz) toward optimal spectral alignment. At the specific value $g_4 = \sqrt{2}d_5/7$, we achieved exact phase matching

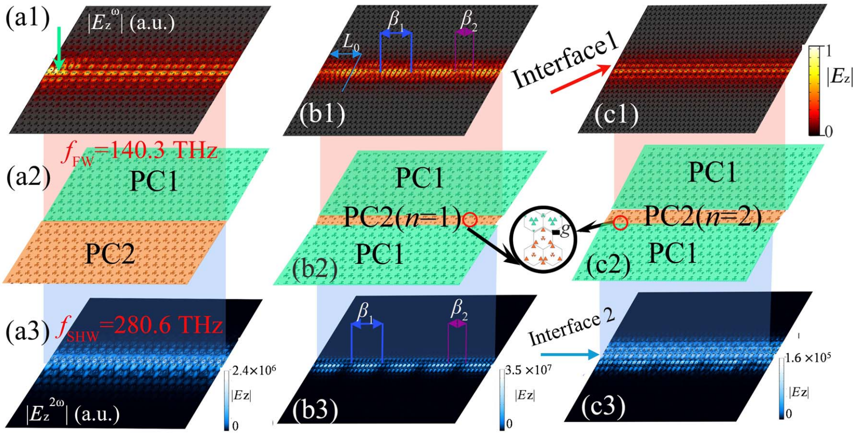

Fig. 4. Simulation of FW and SHW in sandwich photonic crystals. (a1)–(c1) Amplitudes of FW. (a2)–(c2) Sandwich structure with different n. (a3)–(c3) Amplitudes of SHW. $\beta_1 = 7a$, $\beta_2 = 4a$, indicate the lengths for the high/low conversion regions of SHG, respectively. $L_0 = 17a$.

where $2f_{\mathrm{FW}} = f_{\mathrm{SHW}} = 280.6$ THz, enabling simultaneous high-efficiency transmission and frequency separation of FW and SHW through distinct propagation channels.

We validated the design using time-domain simulations with point-source excitation $E(\omega) = E_0 \sin(\omega t)$, where $E_0 = 3 \times 10^9$ V/m and $\omega = 2\pi f_{\mathrm{FW}}$, where $f_{\mathrm{FW}} = 140.3$ THz. Figures 4(a1)–4(a3) show the calculated results of FW [Fig. 4(a1)] and the generated SHW [Fig. 4(a3)] at the interface of PC1 and PC2. The SHG conversion efficiency is $\eta = 19.8\%\ \mathrm{W}^{-1}\,\mathrm{cm}^{-2}$. For comparison, two sandwich structures with PC2 layer numbers of $n = 1$ and $n = 2$ were investigated. For $n = 1$ [Fig. 4(b)], the structure achieved FW transmission efficiency exceeding 99.66% [Fig. 4(b1)] while maintaining the highest SHG conversion efficiency of $\eta = P_{\mathrm{SHW}}/(P_{\mathrm{FW}}^2 \cdot L_0^2) = 139.4\%\ \mathrm{W}^{-1}\,\mathrm{cm}^{-2}$ [Fig. 4(b3)]—even slightly higher than the SHG efficiency observed in dual-resonance topological PhCs [30], where P_{FW} is the input power of FW and P_{SHW} is the power of SHW at L_0, respectively. For $n = 2$ [Fig. 4(c)], the structure yielded a lower conversion efficiency of $\eta = 1.81\%\ \mathrm{W}^{-1}\,\mathrm{cm}^{-2}$ [Fig. 4(c3)] due to increased separation between two interfaces. Both configurations ($n = 1$, $n = 2$) maintained frequency separation without phase-mismatch oscillations, contrasting with resonance-limited approaches [38,39].

4. TOPOLOGICAL SEPARATION DEVICE

Based on the above research and analysis, we designed an SHG frequency-doubling and separation device. As shown in Fig. 5(a), the monolithic frequency divider implementation [Fig. 5(a)] integrates SHG and demultiplexing functionalities within a unified photonic circuit. The architecture features PC2 crystals symmetrically arranged around PC1, with the front section dedicated to nonlinear conversion and the rear section routing signals through 60°-angled output ports.

We introduce two key parameters to characterize device performance: separation efficiency and crosstalk suppression. The separation efficiency is defined as the ratio of correctly routed optical power to the target output port versus the total input power before signal separation, with specific formulations for each wavelength component: $\eta_{\mathrm{sep}} = P_{\mathrm{FW}}^{\mathrm{Port2}}/P_{\mathrm{FW}}$ for FW and $\eta_{\mathrm{sep}} = P_{\mathrm{SHW}}^{\mathrm{Port3}}/P_{\mathrm{SHW}}$ for SHW, where P_{FW} and P_{SHW} represent optical powers measured before signal separation, while $P_{\mathrm{FW}}^{\mathrm{Port2}}$ and $P_{\mathrm{SHW}}^{\mathrm{Port3}}$ denote powers measured at the designated output ports. Crosstalk suppression quantifies interference between channels, calculated as $\zeta_{\mathrm{Port2}} = 10 \times \log_{10}(P_{\mathrm{SHW}}^{\mathrm{Port2}}/P_{\mathrm{FW}}^{\mathrm{Port2}})$ in dB for SHW suppression in the FW channel and $\zeta_{\mathrm{Port3}} = 10 \times \log_{10}(P_{\mathrm{FW}}^{\mathrm{Port3}}/P_{\mathrm{SHW}}^{\mathrm{Port3}})$ in dB for FW suppression in the SHW channel.

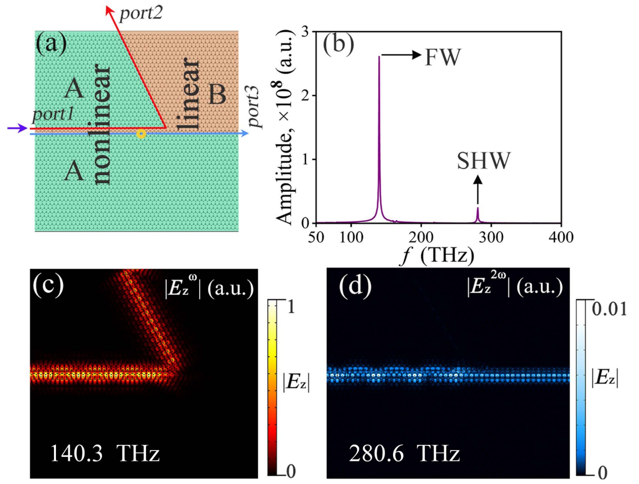

Fig. 5. Simulation of the topological photonic nonlinear double frequency divider. (a) The structure. (b) Detected frequency spectra. (c) Amplitude of the electric field of FW. (d) Amplitude of the electric field of SHW.

Calculated performance characterization demonstrated greater than 99.88% separation efficiency between FWs (directed to Port 2 via topological edge states) and SHWs (routed to Port 3 through trivial boundary modes), realizing a minimum crosstalk suppressions of −29.2 dB at $f_2 = 280.46$ THz (without an air gap) throughout the full operational bandwidth of ±1.19 THz. This performance matches the state-of-the-art in topological isolation systems [40,41] while simultaneously enabling second-harmonic generation—a dual-functionality capability unattained in previous topological platforms. Moreover, this monolithic integration of SHG and wavelength separation within a single compact circuit overcomes the hybrid-component limitations of conventional beam splitters [21,42], eliminating insertion losses that typically degrade quantum light sources. By enabling simultaneous nonlinear generation and demultiplexing, our platform establishes a scalable approach for on-chip quantum frequency conversion and wavelength-division multiplexing systems [43].

5. CONCLUSION

In summary, our work establishes the first monolithic platform integrating topological SHG and wavelength demultiplexing by unifying air-gap dispersion tuning ($g_4 = \sqrt{2}d_5/7$), dual-boundary state control, and chiral routing in a single photonic circuit. Maximum second-harmonic generation efficiency of 139.4% $\mathrm{W}^{-1}\,\mathrm{cm}^{-2}$ is achieved when the number of lattice layers in the core region is $n = 1$, and spatial isolation of FW/SHW outputs with minimum crosstalk suppression of −29.2 dB maintains across ±1.19 THz operational bandwidth. Therefore, this study offers new insights for developing topological nonlinear photonic devices and enabling scalable nonlinear processors for wavelength-division multiplexing and frequency-encoded quantum systems.

APPENDIX A: PHASE DISTRIBUTIONS OF BANDS 4, 5 AND THE BERRY PHASE

We simultaneously investigated the high-frequency band properties of PC1 and PC2. The two types of unit cell structures are $d_2 = 0.27a, l_2 = 0.2a$, as shown in Fig. 6(a), and $d_1 = 0.2a$, $l_1 = 0.27a$, , as shown in Fig. 6(b). The fourth band's phase distributions of E_z at K are shown in Figs. 6(a1) and 6(b1); the phase of the fifth band is shown in Figs. 6(a2) and 6(b2). In both cases, the phase distribution did not change, and there was no phase inversion.

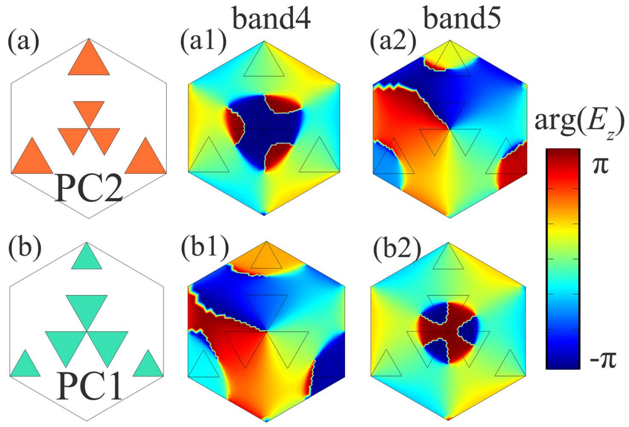

Fig. 6. The phase relationship between the fourth and fifth bands of the two structures. (a), (b) Unit cell structures. (a1), (a2) Calculated phases of the fourth and fifth bands at K (K') in Fig. 1(b2) with cell parameters of (d_2, l_2). (b1), (b2) Calculated phases of the fourth and fifth bands at K (K') in Fig. 1(b2) with cell parameters of (d_1, l_1).

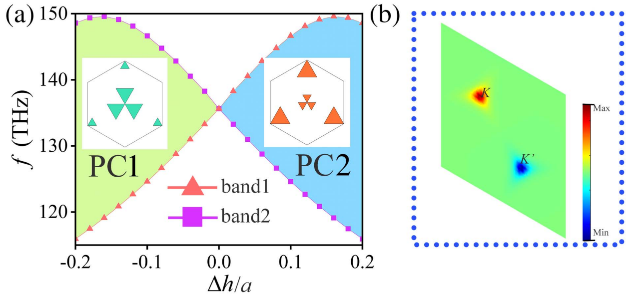

Fig. 7. Topological properties of bands 1 and 2. (a) Frequency evolution at the K point versus structural asymmetry parameter Δh for band 1 (triangles) and band 2 (squares). (b) Calculated Berry phase for parameters $d_2 = 0.27a$ and $l_3 = 0.12a$.

Quantitative investigation of $\Delta h = d - l$ reveals critical bandgap tuning mechanisms [Fig. 7(a)]. When $d = d_2 = 0.27a$ and $l = l_3 = 0.12a$, the first band occupies a lower frequency position while the second band resides at higher frequencies. As Δh increases and the parameters invert to $d = l_3 = 0.12a$, $l = d_2 = 0.27a$, the first and second bands undergo frequency crossing—designated as the PC1 phase transition point. Further calculated Berry phase analysis confirms the topological nontrivial characteristics. The Berry phase $\gamma_n = \oint_{\mathrm{FBZ}} \mathcal{A}_n(k) \cdot \mathrm{d}k$, where $\mathcal{A}_n(k) = \langle E_n(k)|i\nabla_k|E_n(k)\rangle$ denotes Berry connection, quantifies this distinction. As shown in Fig. 7(b) for the configuration $d_2 = 0.27a$, $l_3 = 0.12a$, the Berry phases between K and K′ exhibit opposite signs for the first and second bands, confirming nontrivial topology.

APPENDIX B: CALCULATED DISPERSION CURVES IN PC1-PC2 AND PC2-PC1-PC2

Figure 8 shows two additional types of topological edge states and ordinary boundary states. Figure 8(a) illustrates the ordinary boundary state of the second bandgap at the PC2-

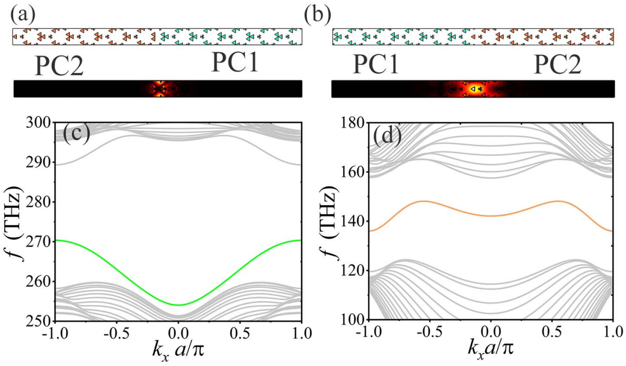

Fig. 8. Calculated dispersion curves and transmission when $(d_2, l_3) = (0.27a, 0.12a)$. (a), (b) Supercells. (c) The dispersion curves of the second band for (a). (d) The dispersion curves of the first band for (b).

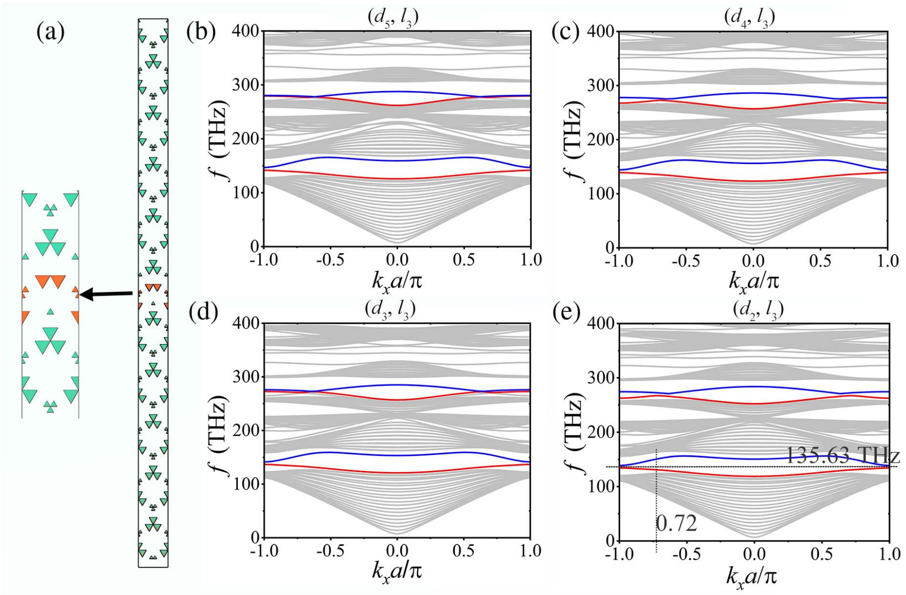

Fig. 9. Calculated band dispersions of the sandwich structure. (a) The sandwich supercell. (b)–(e) The corresponding dispersion relations for different d and l values, respectively.

PC1 interface, as indicated by the green line in Fig. 8(c). Figure 8(b) depicts the topological boundary state of the first bandgap at the PC1-PC2 interface, as shown by the orange line in Fig. 8(d). The electric field patterns are shown in the middle. It is observed that both types of edge states are localized at the designed interfaces. This effect determines the separation of the fundamental frequency and the second harmonic.

In Fig. 9, we present the band dispersion relations of the sandwich-type structure with the following parameters: $l_3 = 0.12a$ and d varying as $d_5 = 0.24a$, $d_4 = 0.25a$, $d_3 = 0.26a$ and $d_2 = 0.27a$.

APPENDIX C: SIMULATION RESULTS OF THE SANDWICH STRUCTURE AND FREQUENCY SPECTRA

We compared the PC1-PC2 interface shown in Fig. 8(a) with the sandwich-type PC1-PC2-PC1 structure shown in Fig. 9(a). For the PC1-PC2 structure, at the interface, the fundamental frequency $f_{\mathrm{FW}} = 135.63$ THz and second-harmonic frequency $f_{\mathrm{SHW}} = 271.4$ are shown in Figs. 10(a1) and 10(a3). For the sandwich structure, Fig. 10(a2), its nearby frequencies can exist as interface states, but in the sandwich structure [Fig. 8(d)], the fundamental frequency and its second harmonic in the sandwich structure show that the fundamental frequency lies precisely within the bandgap. Since no propagating modes exist in this frequency range, the fundamental wave becomes completely non-propagating.

In Fig. 11, we present the electric field amplitudes of the fundamental frequency and the second harmonic under three structures in the main text (Fig. 4, $d_5 = 0.24a$, $l_3 = 0.12a$), observing the second-harmonic generation in all cases.

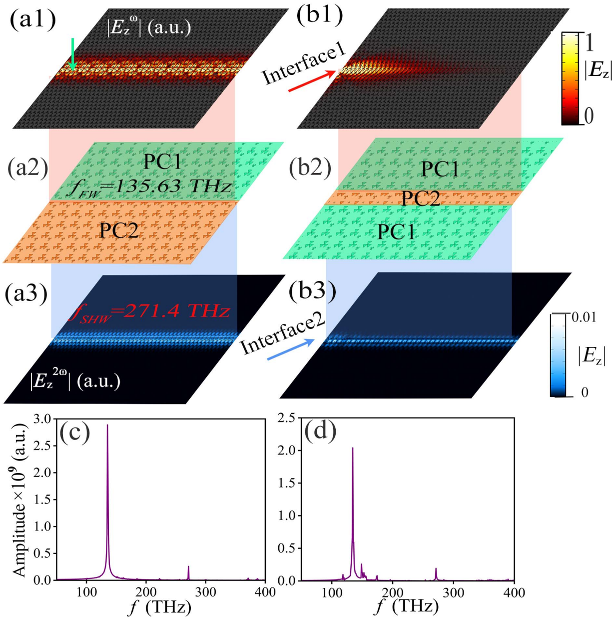

Fig. 10. Simulation results of the sandwich structure. (a1), (b1) Amplitude of SW. (a2), (b2) Sandwich structure with different n. (a3), (b3) Amplitude of SHW. (c), (d) The spectral distributions of the PC1-PC2-type and PC1-PC2-PC1-type structures calculated.

APPENDIX D: OPTIMIZATION RESULTS UNDER DIFFERENT *d*

Figure 12 illustrates the linear propagation of FW modes in photonic crystals with three sets of structural parameters without an air gap $g_5 = 0$. The size of the pillar d is adjusted to

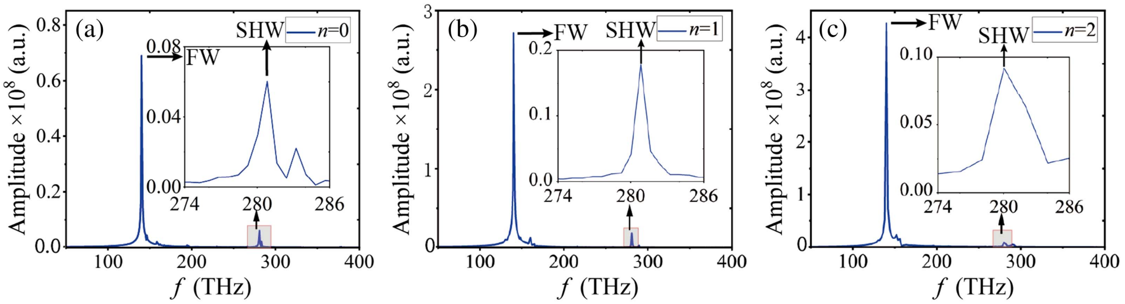

Fig. 11. Detected frequency spectra for the (a) first, (b) second, and (c) third columns, respectively.

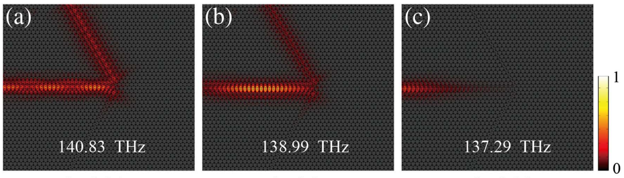

d_5=0.24a d_4=0.25a d_3=0.26a

Fig. 12. Linear propagation of FW in photonic crystal with 60° bent interface. (a)–(c) Structures with the pillar sizes of d_5, d_4, and d_3, respectively.

$d_5 = 0.24a$, $d_4 = 0.25a$, and $d_3 = 0.26a$. One can observe that the light field oscillates along the x direction: the oscillation period increases with d, and the SHG efficiency reaches its minimum when $d = d_3$. Therefore, such types of configuration must be optimized further.

Funding. National Natural Science Foundation of China (12174307).

Disclosures. The authors declare no conflicts of interest.

Data Availability. Data underlying the results presented in this paper are not publicly available at this time but may be obtained from the authors upon reasonable request.

REFERENCES

1. L. W. Luo, N. Ophir, C. P. Chen, *et al.*, "WDM-compatible mode-division multiplexing on a silicon chip," Nat. Commun. **5**, 3069 (2014).
2. X. Qiao, Y. Li, Y. Liu, *et al.*, "Inverse-designed multidimensional-division-multiplexing photonic circuits for dense integration," ACS Photonics **12**, 3256–3264 (2025).
3. A. Liu, L. Liao, Y. Chetrit, *et al.*, "Wavelength division multiplexing based photonic integrated circuits on silicon-on-insulator platform," IEEE J. Sel. Top. Quantum Electron. **16**, 23–32 (2010).
4. H. Liu, B. Pan, Y. Huang, *et al.*, "Ultra-compact lithium niobate photonic chip for high-capacity and energy-efficient wavelength-division-multiplexing transmitters," Light Adv. Manuf. **4**, 133 (2023).
5. J. Wang, F. Sciarrino, A. Laing, *et al.*, "Integrated photonic quantum technologies," Nat. Photonics **14**, 273–284 (2020).
6. T. Udem, R. Holzwarth, and T. Hänsch, "Optical frequency metrology," Nature **416**, 233–237 (2002).
7. Y. Yin, H. Yu, D. Tu, *et al.*, "A silicon-based on-chip 64-channel hybrid wavelength- and mode-division (de)multiplexer," Photonics **10**, 183 (2023).
8. M. Z. Hasan and C. L. Kane, "Colloquium: topological insulators," Rev. Mod. Phys. **82**, 3045–3067 (2010).
9. L. Lu, J. D. Joannopoulos, and M. Soljačić, "Topological photonics," Nat. Photonics **8**, 821–829 (2014).
10. T. Ozawa, H. M. Price, A. Amo, *et al.*, "Topological photonics," Rev. Mod. Phys. **91**, 015006 (2019).
11. Z. Wang, Y. Chong, J. D. Joannopoulos, *et al.*, "Observation of unidirectional backscattering-immune topological electromagnetic states," Nature **461**, 772–775 (2009).
12. S. Raghu and F. D. M. Haldane, "Analogs of quantum-Hall-effect edge states in photonic crystals," Phys. Rev. A **78**, 033834 (2008).
13. J. Wang, H. Li, Y. Ma, *et al.*, "Routing valley exciton emission of a WS_2 monolayer via delocalized Bloch modes of in-plane inversion-symmetry-broken photonic crystal slabs," Light Sci. Appl. **9**, 148 (2020).
14. Y. Mao, Z. Li, W. Hu, *et al.*, "Topological slow light rainbow trapping and releasing based on gradient valley photonic crystal," J. Lightwave Technol. **40**, 5152–5156 (2022).
15. W. Zhu, Y. Long, H. Chen, *et al.*, "Quantum valley Hall effects and spin-valley locking in topological Kane-Mele circuit networks," Phys. Rev. B **99**, 115410 (2019).
16. F. Ding, Y. Mao, J. Shen, *et al.*, "Simultaneous slow light and sound rainbow trapping in phoxonic crystals," Opt. Lett. **47**, 5650–5653 (2022).
17. Y. Li, Y. Yu, F. Liu, *et al.*, "Topology-controlled photonic cavity based on the near-conservation of the valley degree of freedom," Phys. Rev. Lett. **125**, 213902 (2020).
18. M. Kim, Z. Jacob, and J. Rho, "Recent advances in 2D, 3D and higher-order topological photonics," Light Sci. Appl. **9**, 130 (2020).
19. Z. Wang, L. Ye, Z. Pu, *et al.*, "Higher-order topological transport protected by boundary Chern number in phononic crystals," Commun. Phys. **7**, 193 (2024).
20. P. Zhang, L. Fang, Y. Zhang, *et al.*, "Topological valley-locked silicon photonic crystal waveguides," Photonics Res. **13**, 2718–2724 (2025).
21. P. Zhang, J. Zhang, L. Gu, *et al.*, "Compact on-chip power splitter based on topological photonic crystal," Opt. Mater. Express **14**, 1390–1397 (2024).
22. L. Gu, Q. Yuan, Q. Zhao, *et al.*, "A topological photonic ring-resonator for on-chip channel filters," J. Lightwave Technol. **39**, 5069–5073 (2021).
23. Q. Yuan, L. Gu, L. Fang, *et al.*, "Giant enhancement of nonlinear harmonic generation in a silicon topological photonic crystal nanocavity chain," Laser Photonics Rev. **16**, 2100269 (2022).
24. L. Gu, B. Wang, Q. Yuan, *et al.*, "Fano resonance from a one-dimensional topological photonic crystal," APL Photonics **6**, 086105 (2021).
25. Z. Lan, J. W. You, and N. C. Panoiu, "Nonlinear one-way edge-mode interactions for frequency mixing in topological photonic crystals," Phys. Rev. B **101**, 155422 (2020).
26. Z. Lan, J. W. You, Q. Ren, *et al.*, "Second-harmonic generation via double topological valley-Hall kink modes in all-dielectric photonic crystals," Phys. Rev. A **103**, L041502 (2021).
27. K. Guo, J. Wu, F. Chen, *et al.*, "Second harmonic generation enhancement and directional emission from topological corner state based

on the quantum spin Hall effect," Opt. Express **29**, 26841–26850 (2021).

28. Y. Chen, Z. Lan, J. Li, *et al.*, "Topologically protected second harmonic generation via doubly resonant high-order photonic modes," Phys. Rev. B **104**, 155421 (2021).
29. K. Guo, H. Wang, J. Xiong, *et al.*, "Shape unrestricted topological corner state based on Kekulé modulation and enhanced nonlinear harmonic generation," Nanophotonics **13**, 3485–3494 (2024).
30. W. Hu, C. Liu, J. Guo, *et al.*, "Topological slow light enhanced second harmonic generation in double-resonant topological photonic crystal," J. Appl. Phys. **134**, 113102 (2023).
31. Y. Chen, P. Zuo, T. Shi, *et al.*, "Photonic-based reconfigurable microwave frequency divider using two cascaded dual-parallel Mach-Zehnder modulators," Opt. Express **28**, 30797–30809 (2020).
32. Y. Wang, X. Li, J. Wo, *et al.*, "Photonic frequency division of broadband microwave signal based on a Fourier domain mode-locked optoelectronic oscillator," Opt. Laser Technol. **147**, 107704 (2022).
33. A. Fernández-Hinestrosa, J. M. Luque-González, P. Cheben, *et al.*, "Nanophotonic Bragg grating assisted Mach–Zehnder interferometers for O-band add-drop filters," Sci. Rep. **14**, 18492 (2024).
34. A. Othonos, "Fiber Bragg gratings," Rev. Sci. Instrum. **68**, 4309–4341 (1997).
35. A. L. Glebov, O. Mokhun, A. Rapaport, *et al.*, "Volume Bragg gratings as ultra-narrow and multiband optical filters," Proc. SPIE **8428**, 84280C (2012).
36. W. Zhang and J. Yao, "A fully reconfigurable waveguide Bragg grating for programmable photonic signal processing," Nat. Commun. **9**, 1396 (2018).
37. L. Carletti, A. Locatelli, O. Stepanenko, *et al.*, "Enhanced second-harmonic generation from magnetic resonance in AlGaAs nanoantennas," Opt. Express **23**, 26544–26550 (2015).
38. E. Nitiss, J. Hu, A. Stroganov, *et al.*, "Ultra-efficient second harmonic generation via mode phase matching in integrated lithium niobate racetrack resonators," Nat. Photonics **16**, 134–141 (2022).
39. J. Cheng, D. Gao, J. Dong, *et al.*, "Ultra-efficient second harmonic generation via mode phase matching in integrated lithium niobate racetrack resonators," Opt. Express **31**, 36736–36744 (2023).
40. W. Dai, T. Yoda, Y. Moritake, *et al.*, "High transmission in 120-degree sharp bends of inversion-symmetric and inversion-asymmetric photonic crystal waveguides," Nat. Commun. **16**, 796 (2023).
41. X. Wang, Y. Han, H. Fei, *et al.*, "Design of wavelength division multiplexing devices based on tunable edge states of valley photonic crystals," Opt. Express **31**, 13933–13942 (2023).
42. Y.-H. He, Y. Gao, Y. He, *et al.*, "Realization of edge and corner states in photonic crystals with Kagome lattices through topological insulator generators," Opt. Laser Technol. **161**, 109196 (2022).
43. Y. Ruan, X. Qian, H. X. Wang, *et al.*, "Applications for wavelength division multiplexers based on topological photonic crystals," Photonics Res. **11**, 569–574 (2023).